Chapter 10: Global Climate Projections

Coordinating Lead Authors: Gerald A. Meehl, Thomas F. Stocker

Lead Authors: William Collins, Pierre Friedlingstein, Amadou Gaye, Jonathan Gregory, Akio Kitoh, Reto Knutti, James Murphy, Akira Noda, Sarah Raper, Ian Watterson, Andrew Weaver, Zong-Ci Zhao

Contributing Authors: J. Annan, J. Arblaster, C. Bitz, A. le Brocq, P. Brockmann, L. Buja, G. Clarke, M. Collins, E. Driesschaert, N.A. Diansky, K. Dixon, J.-L. Dufresne, M. Dyurgerov, M. Eby, N. Edwards, S. Emori, P. Forster, R. Furrer, J. Hansen, G. Hegerl, M. Holland, A. Hu, P. Huybrechts, F. Joos, J. Kettleborough, M. Kimoto, M. Krynytzky, M.-F. Loutre, J. Lowe, M. Meinshausen, S. Müller, S. Nawrath, J. Oerlemans, T. Palmer, A. Payne, G.-K. Plattner, J. Räisänen, G.L. Russell, A. Rinke , D. Salas y Melia, G. Schmidt, B. Schneider, A. Shepherd, D. Stainforth, C. Tebaldi, H. Teng, L. Terray, A. Sokolov, P. Stott, E. M. Volodin, B. Wang, T. M. L. Wigley, Y. Yu, S. Yukimoto

Review Editors: M. R. Allen, G. B. Pant

Date of Draft: 15 August 2005

Notes: This is the TSU compiled version

Figures

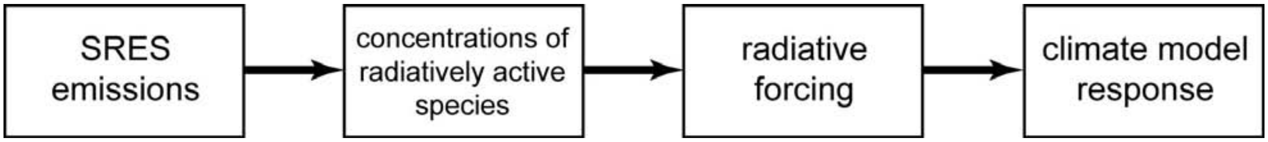

Figure 10.1.1. Various contributions to uncertainty in climate model projections.

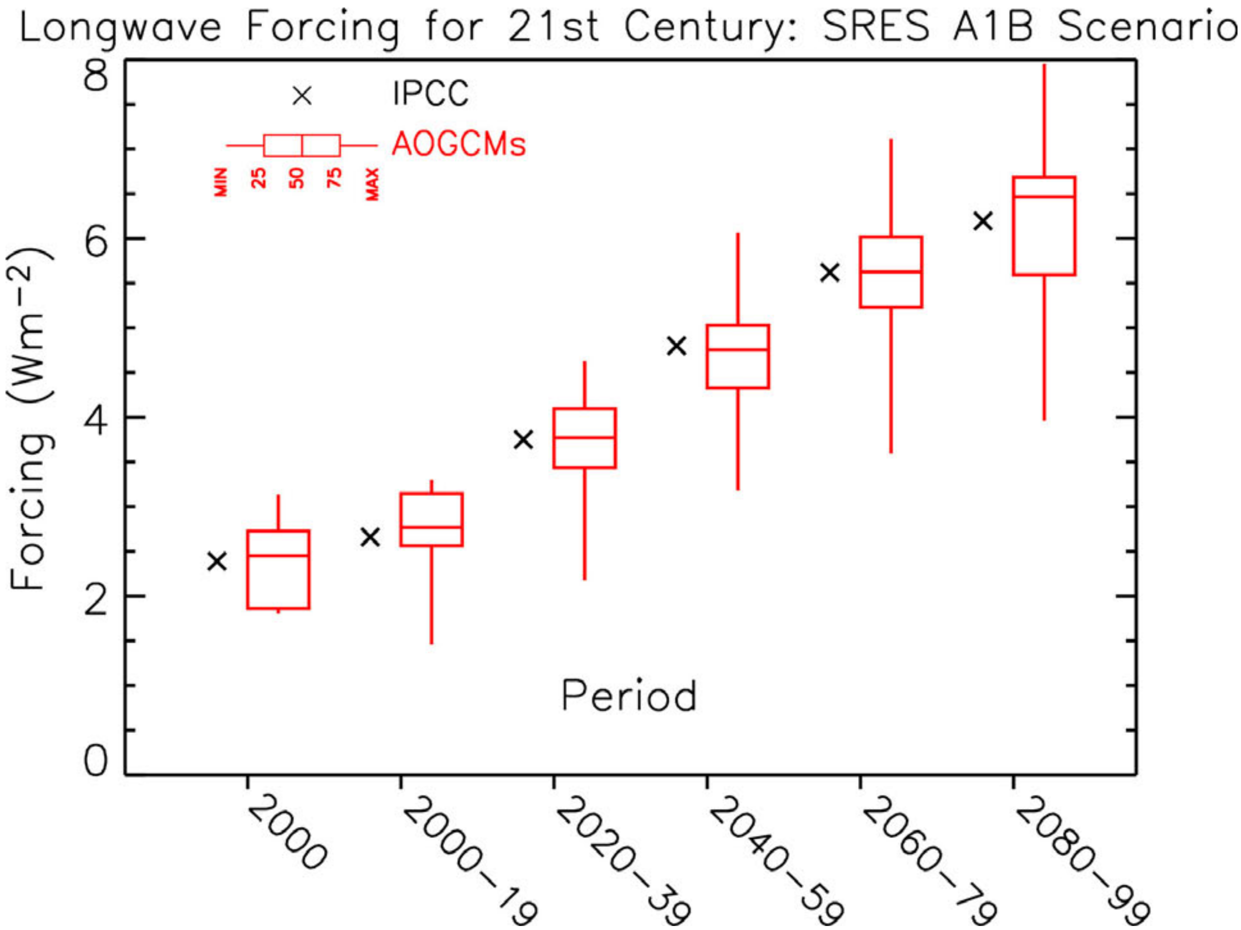

Figure 10.2.1. Longwave forcing for 2000–2100 for the SRES A1B scenario diagnosed from AOGCMs and from the IPCC TAR (2001) forcing formulas (Forster, 2005). The AOGCM results are plotted with box-and-whisker diagrams representing percentiles of forcings from 14 models in the AR4 multi-model ensemble. The AOGCM forcings are computed relative to the starting times of the individual integrations in the 19th century. The IPCC forcings are computed relative to 1850.

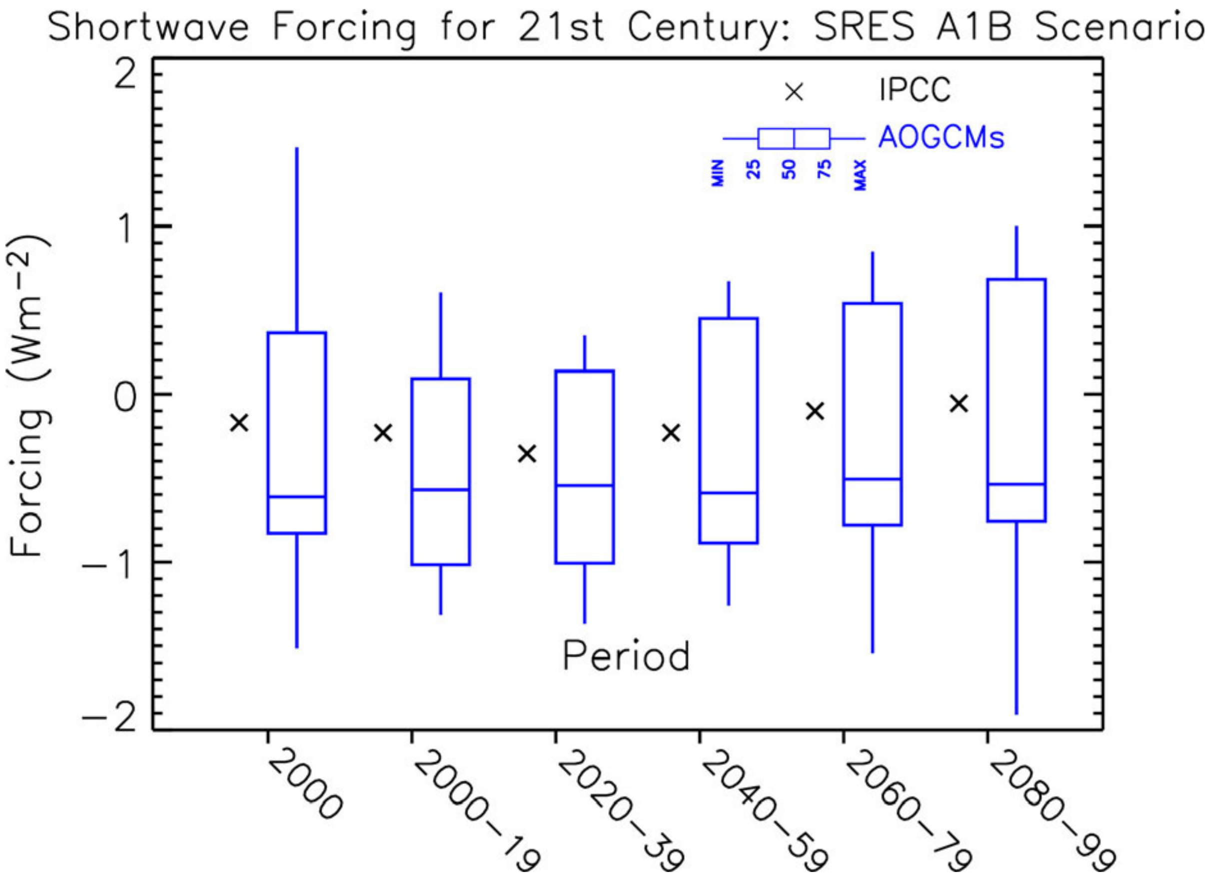

Figure 10.2.2. Shortwave forcing for 2000–2100 for the SRES A1B scenario diagnosed from AOGCMs and from the IPCC TAR (2001) forcing formulas (Forster, 2005). The AOGCM results are plotted with box-and-whisker diagrams representing percentiles of forcings from 14 models in the AR4 multi-model ensemble. The AOGCM forcings are computed relative to the starting times of the individual integrations in the 19th century. The IPCC forcings are computed relative to 1850.

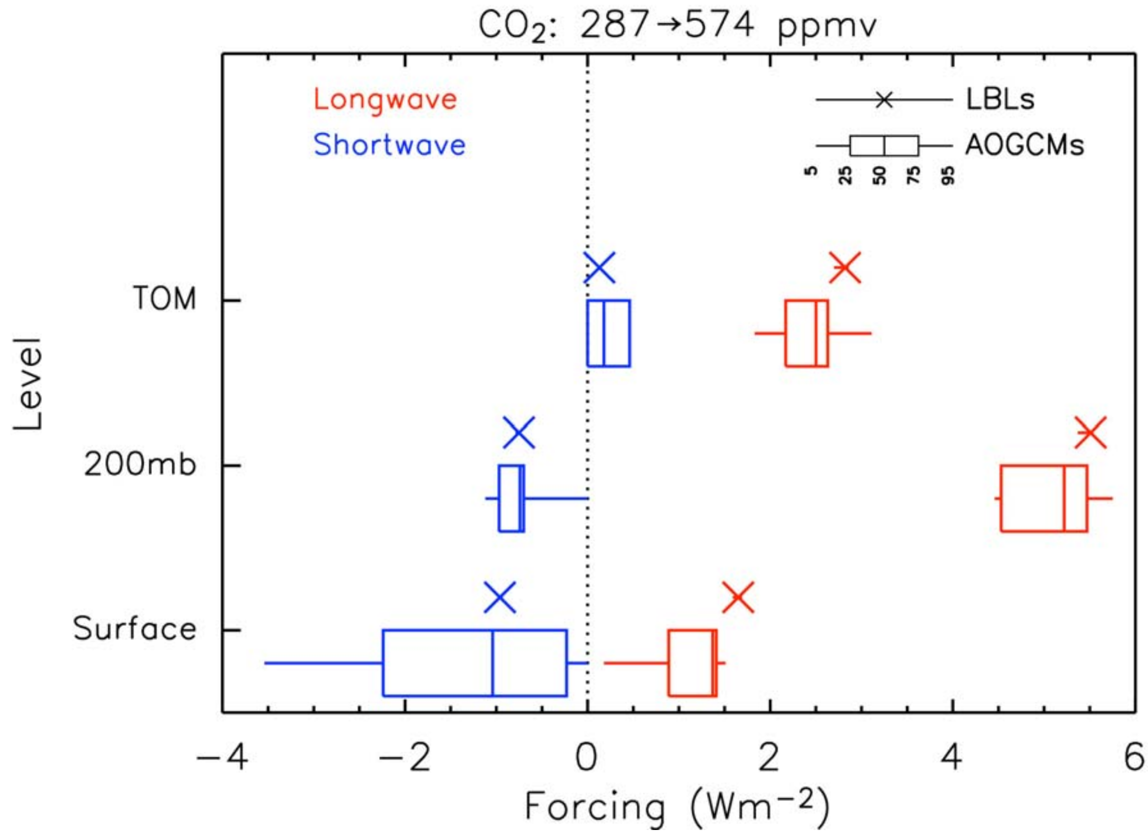

Figure 10.2.3. Comparison of shortwave and longwave radiative forcings for doubling CO_2 from its concentration in 1860 for AOGCMs and line-by-line (LBL) radiative transfer codes (Collins et al., 2005b). Forcings are computed for clear-sky conditions in mid-latitude summer and do not include effects of stratospheric adjustment. No other well-mixed greenhouse gases are included. The AOGCM results are plotted with box-and-whisker diagrams representing percentiles of forcings from 20 models in the AR4 multi-model ensemble. The minimum-to-maximum range and median are plotted for five representative LBL codes.

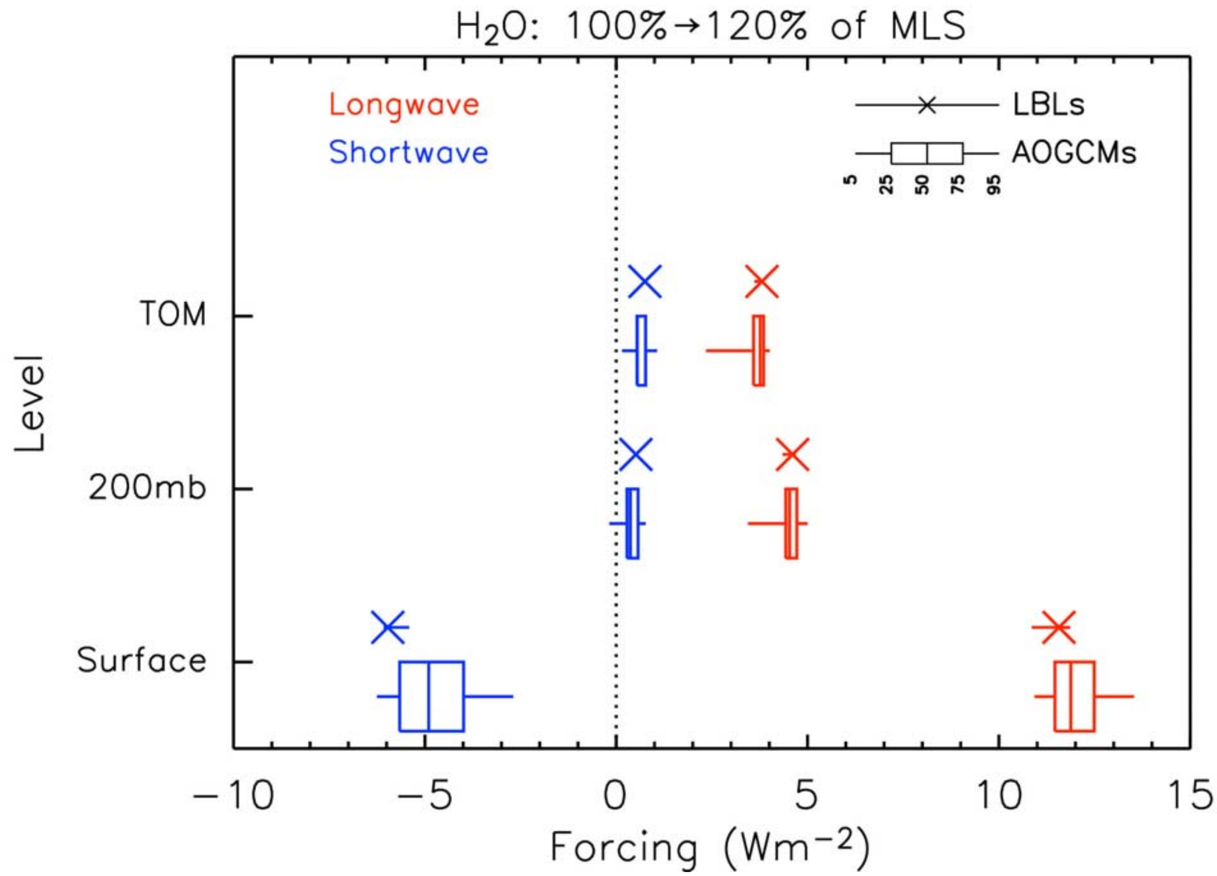

Figure 10.2.4. Comparison of shortwave and longwave radiative forcings from the increase in H2O expected in the climate produced from doubling CO_2 (Collins et al., 2005b). The conditions, symbols, and models are the same as Fig. 10.2.3. The forcings result from increasing concentrations of H2O by 20% throughout the atmospheric column while holding the concentration of CO_2 fixed at 574 ppmv.

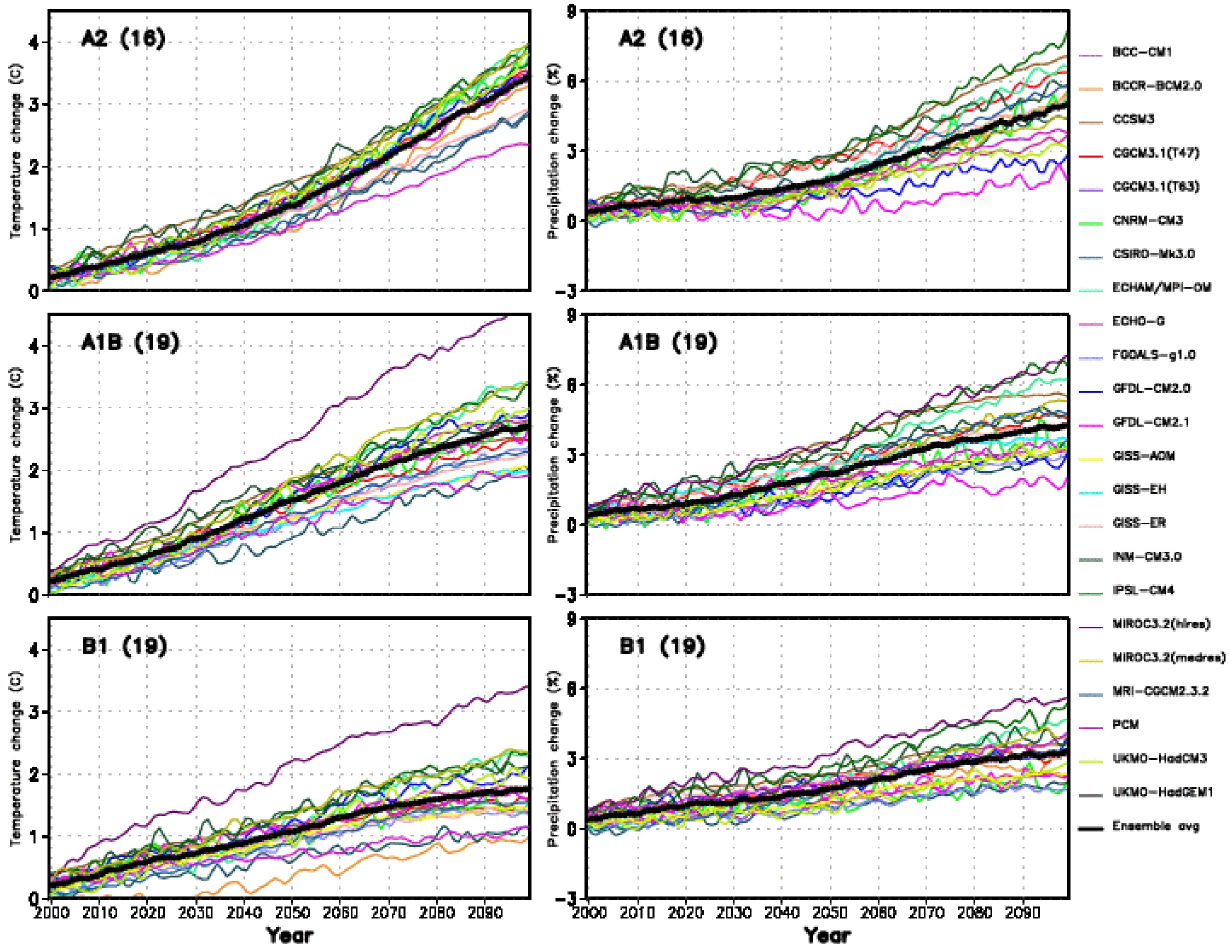

Figure 10.3.1. Time series of globally averaged (left) surface warming (surface air temperature, in °C) and (right) precipitation (in %) from the various global coupled models for the scenarios (top) A2, (middle) A1B and (bottom) B1 scenario. Values are annual means, relative to the 1980–1999 average from the corresponding 20th century simulations, with any linear trends in the corresponding control run simulations removed. Shown in black are the multi-model (ensemble) mean series.

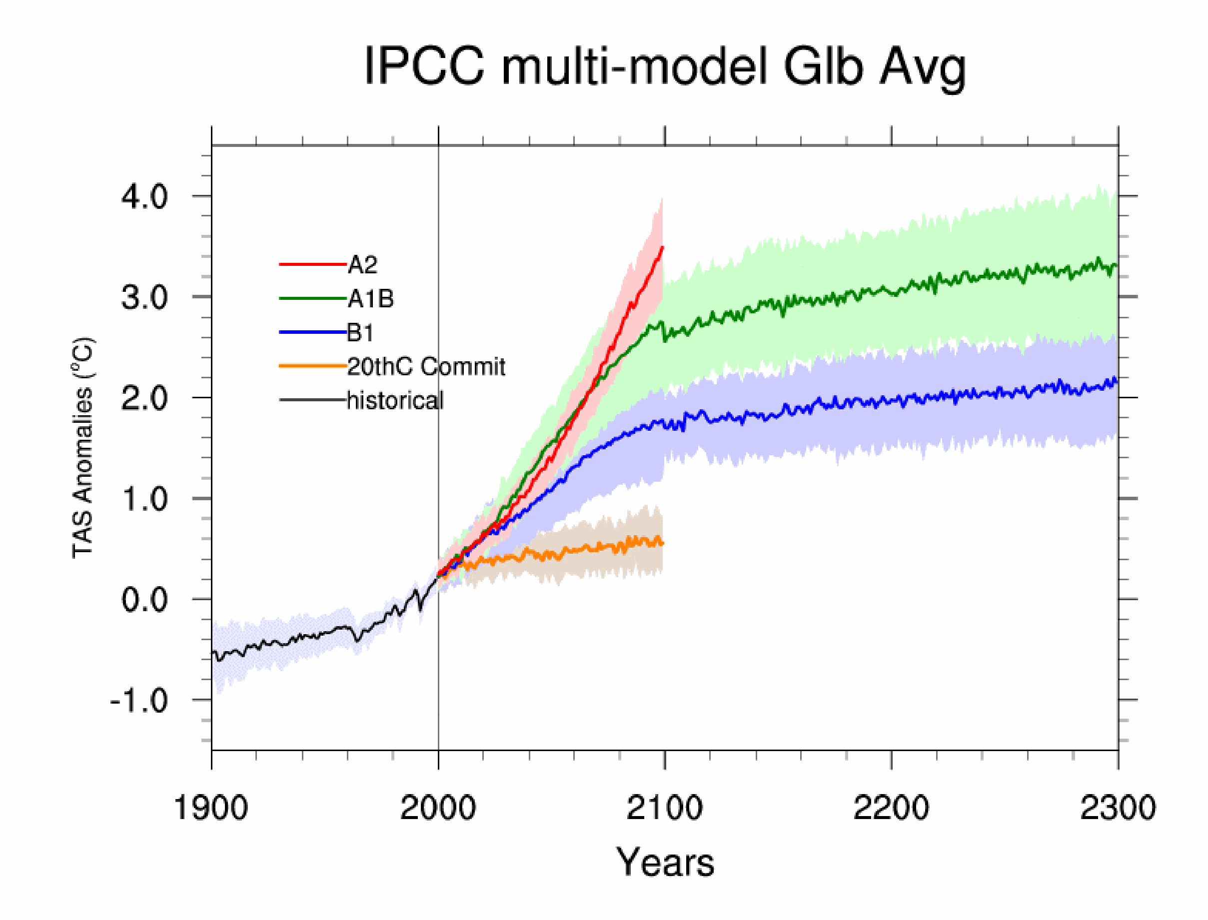

Figure 10.3.2. Multi-model means of surface warming for the scenarios A2, A1B and B1 (as in 10.3.1), shown as continuations of the 20th century simulation. Values beyond 2100 are for the stabilization scenarios (Section 10.7.1). Linear trends from the corresponding control runs have been removed from these time series.

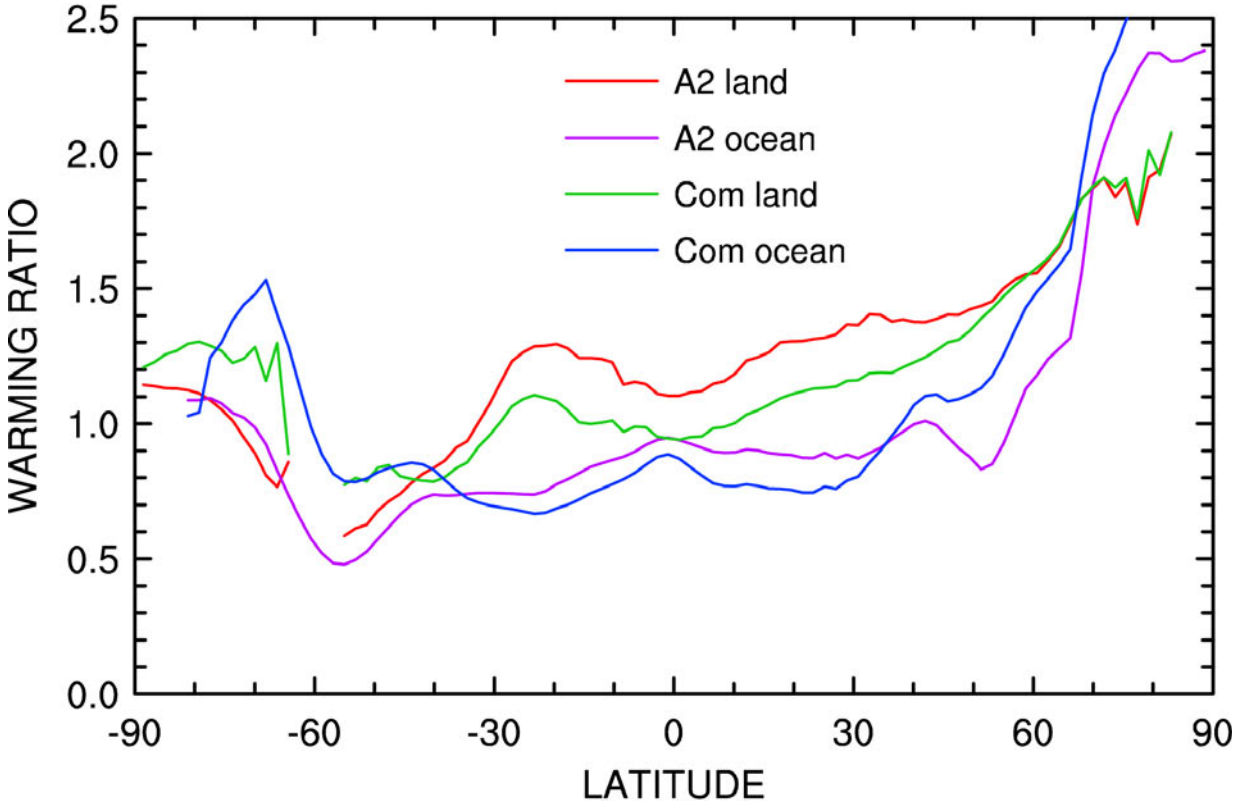

Figure 10.3.3. Zonal means taken over land and ocean separately of annual mean surface warming, shown as a ratio with the global mean warming (Table 10.2). Multi-model mean results are shown for two scenarios, A2 and Commitment (see 10.7), for 2080–2099.

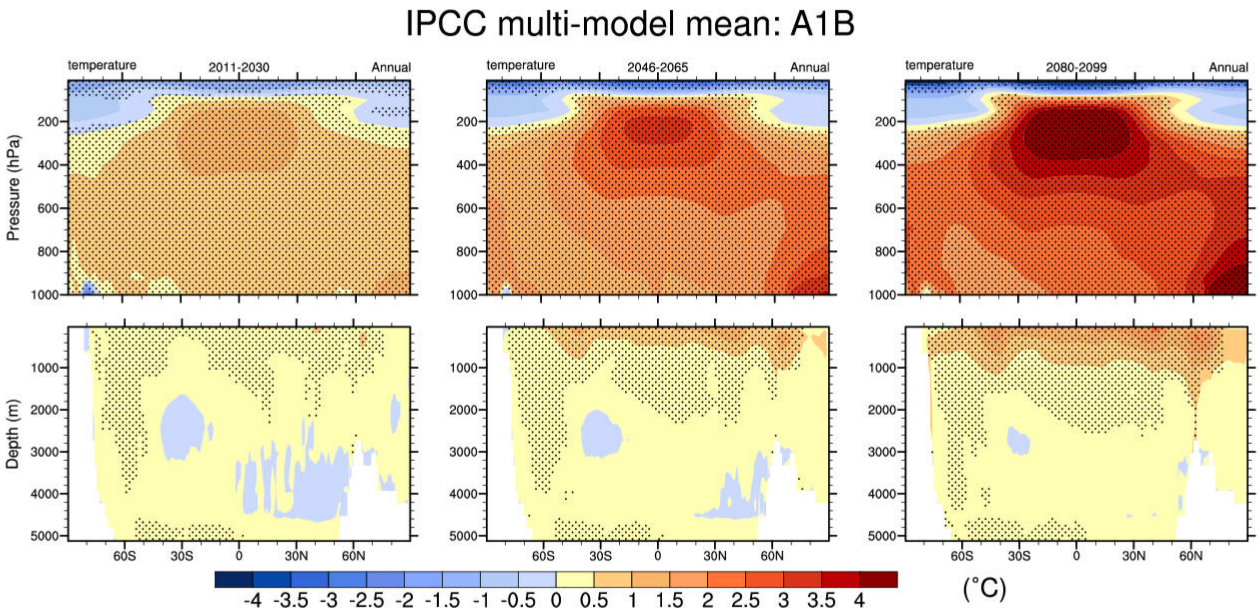

Figure 10.3.4. Zonal means of change in atmospheric and oceanic temperatures, shown as a cross section. Values are the multi-model means for the A1B scenario at each of three periods, as marked. Stippling denotes regions where the multi-model ensemble mean divided by the multi-model standard deviation exceeds 1.0 (in magnitude).

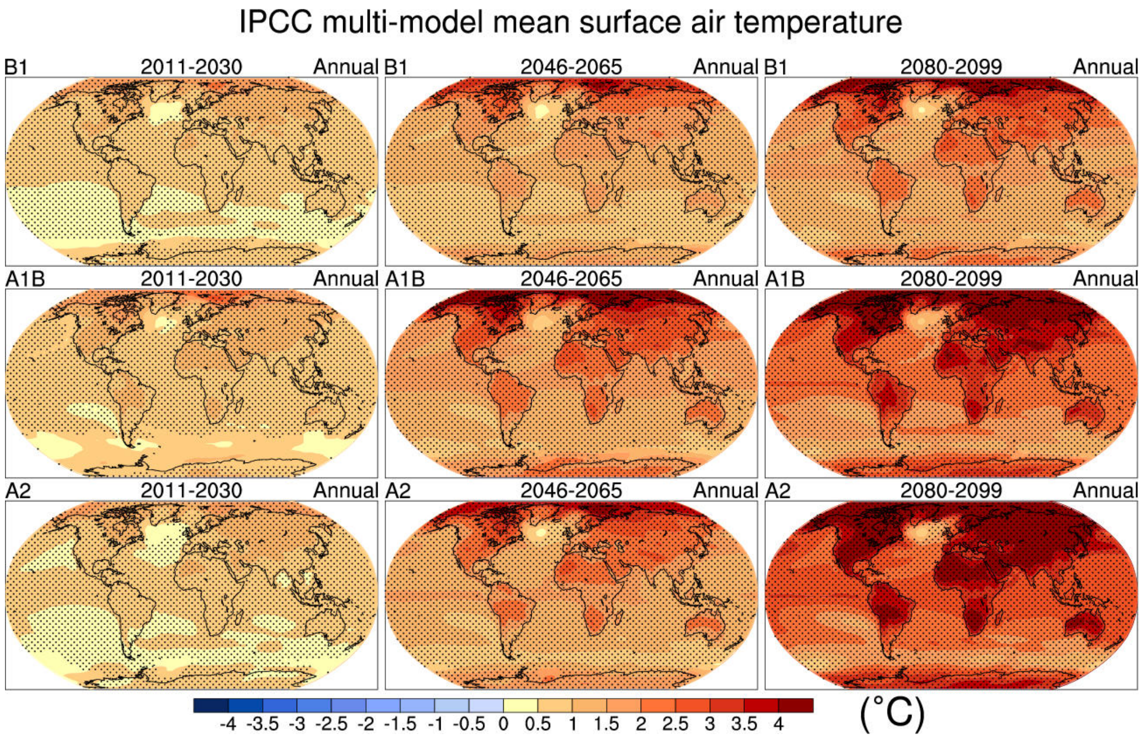

Figure 10.3.5. Multi-model mean of annual mean surface warming (surface air temperature, in °C) for the scenarios (top) B1, (middle) A1B and (bottom) A2, and three time periods, (left) 2011–2030, (middle) 2046–2065, and (right) 2080–2099. Stippling denotes where the multi-model ensemble mean exceeds the intermodel standard deviation.

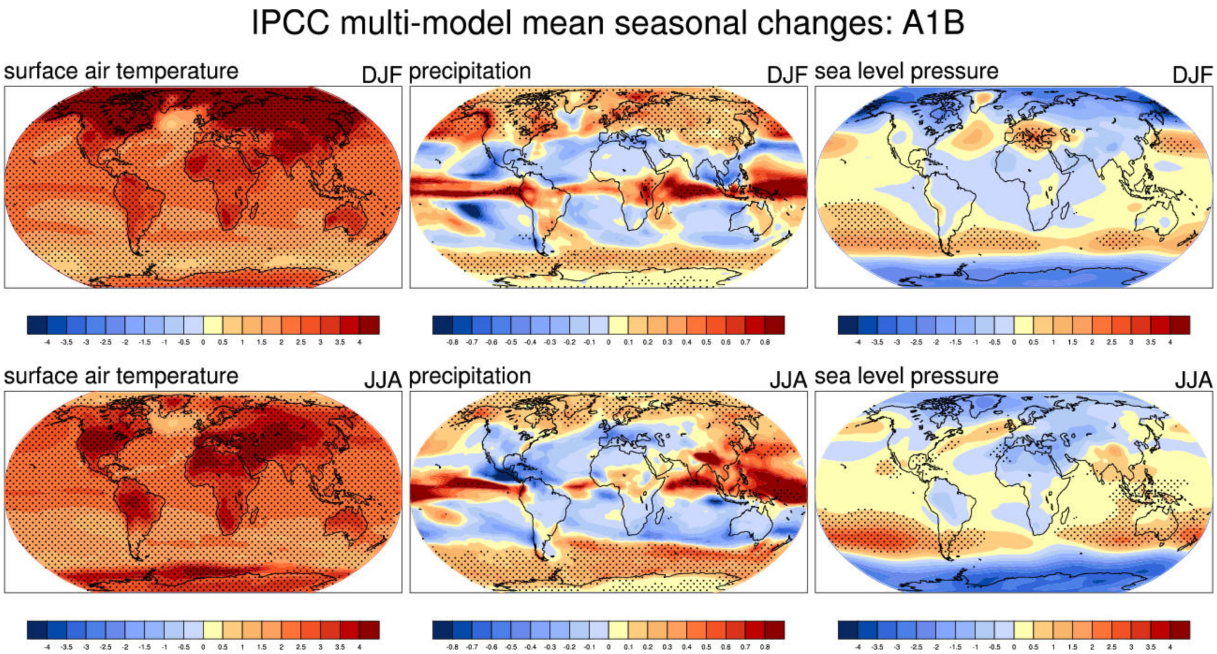

Figure 10.3.6. Multi-model mean change under the A1B scenario for 2080–2099 relative to 1980–1999, for DJF (top) and JJA (bottom). The variables are, from left to right, surface air temperature (°C), precipitation (mm/d), and sea level pressure (hPa). Stippling denotes areas where the magnitude of the multi-model ensemble mean exceeds the inter-model standard deviation.

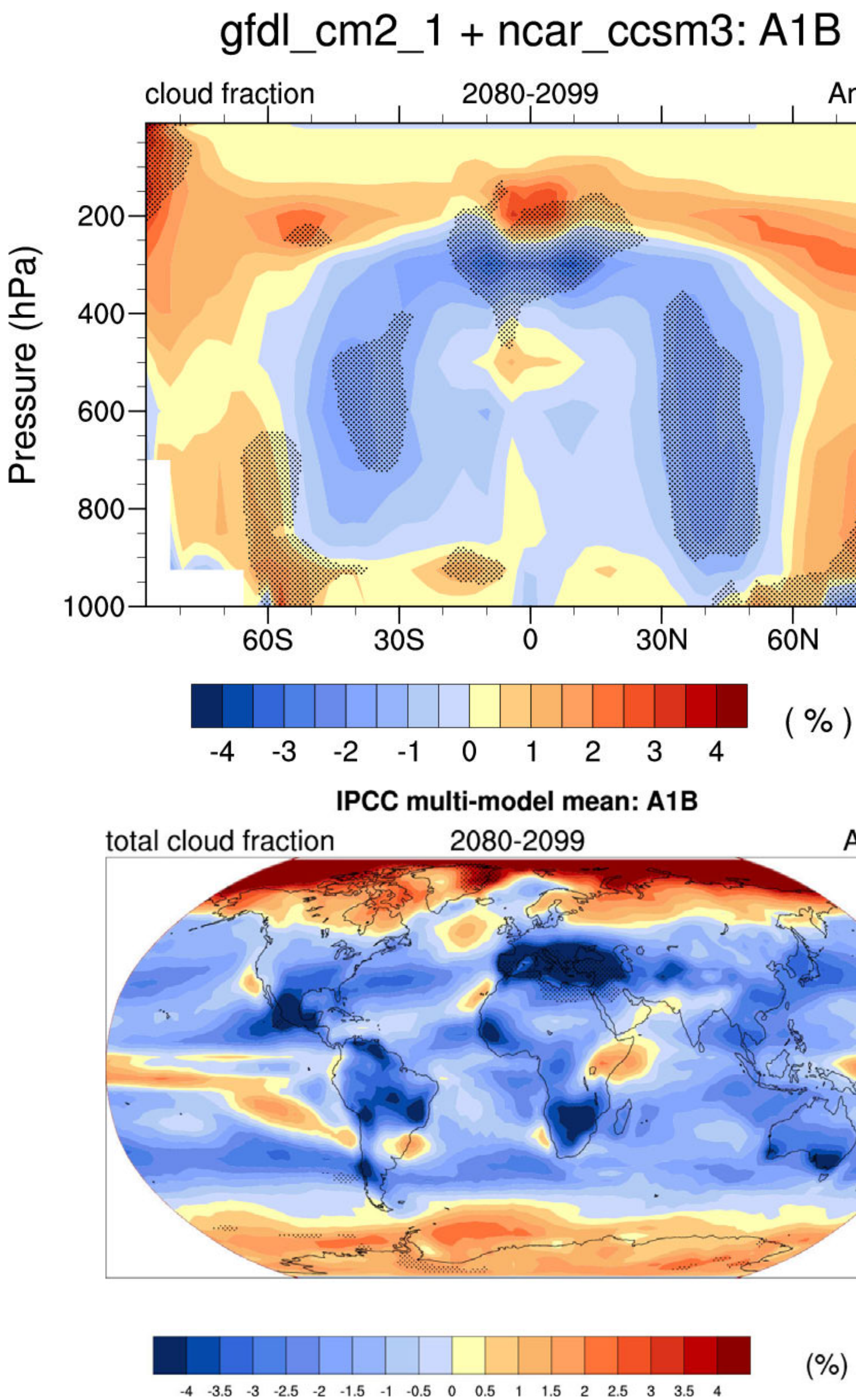

Figure 10.3.7. a) Zonal means of annually averaged change in cloud fraction (in %), shown as a cross section though the atmosphere (data from two models available). b) annually averaged changes in total cloud area fraction (in percentage cover from all models). Values are the multi-model means for the A1B scenario in 2080–2099 relative to 1980–1999.

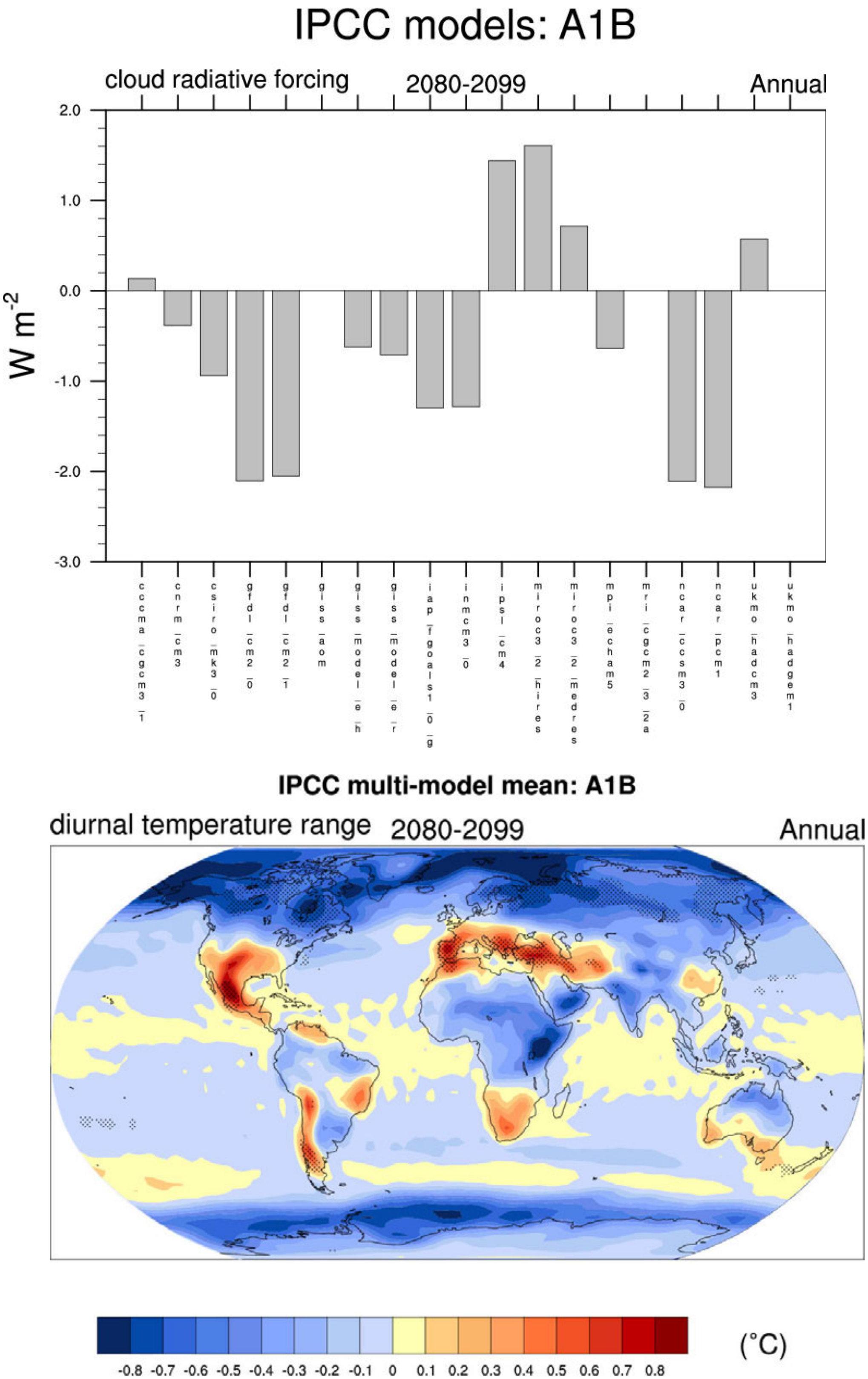

Figure 10.3.8. Annual mean changes under the A1B scenario for 2080–2099 relative to 1980–1999 (a) global mean cloud radiative forcing (in W m^{-2}) from individual models, and (b) multi-model mean DTR (°C)

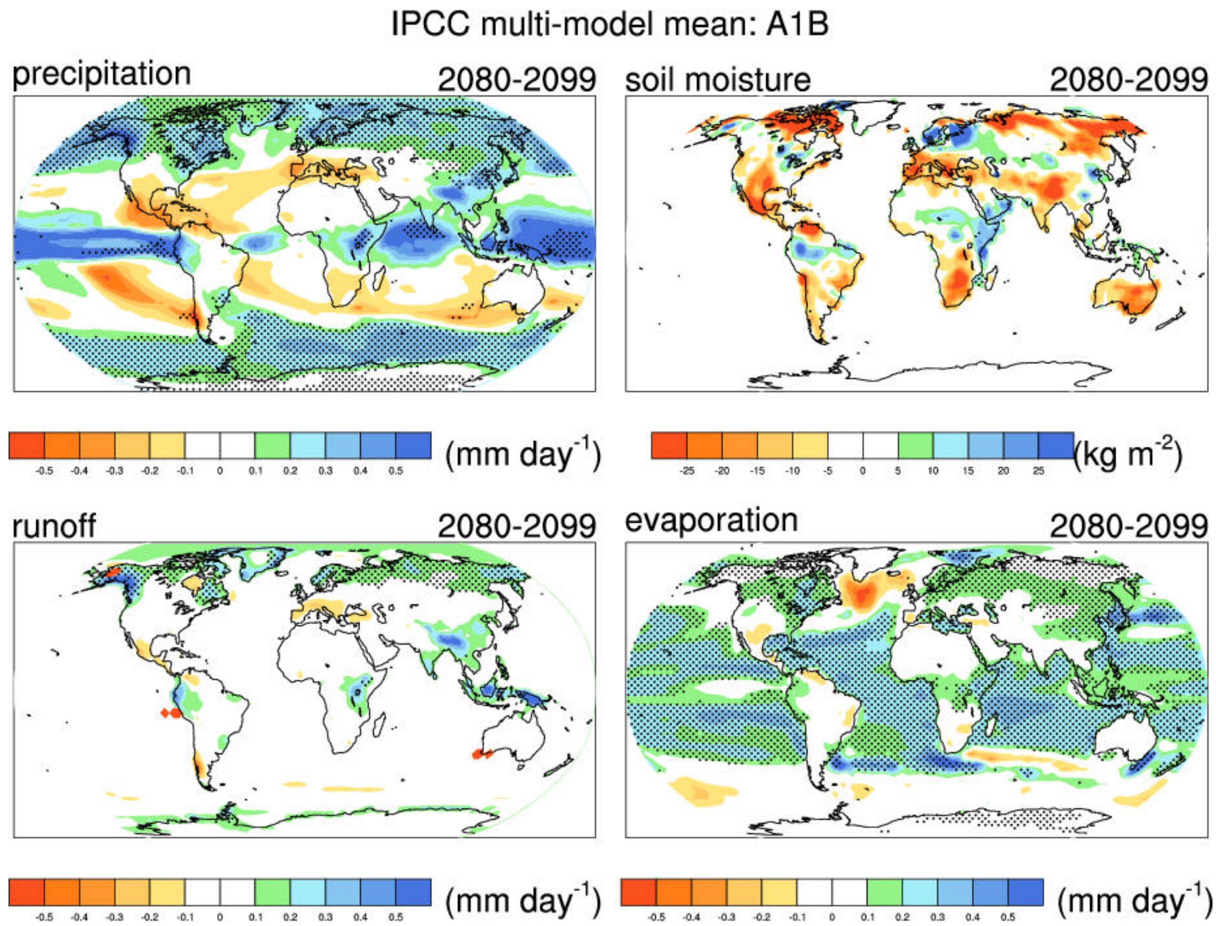

Figure 10.3.9. Multi-model mean change under the A1B scenario for 2080–2099 relative to 1980–1999, for annual means of (a) precipitation, (b) evaporation, (c) runoff (all in mm d^{-1}), and (d) soil moisture content (in kg m^{-2}). Note that "soil moisture content" is the best estimate of this quantity, supplied by each model, but all calculate this quantity somewhat differently.

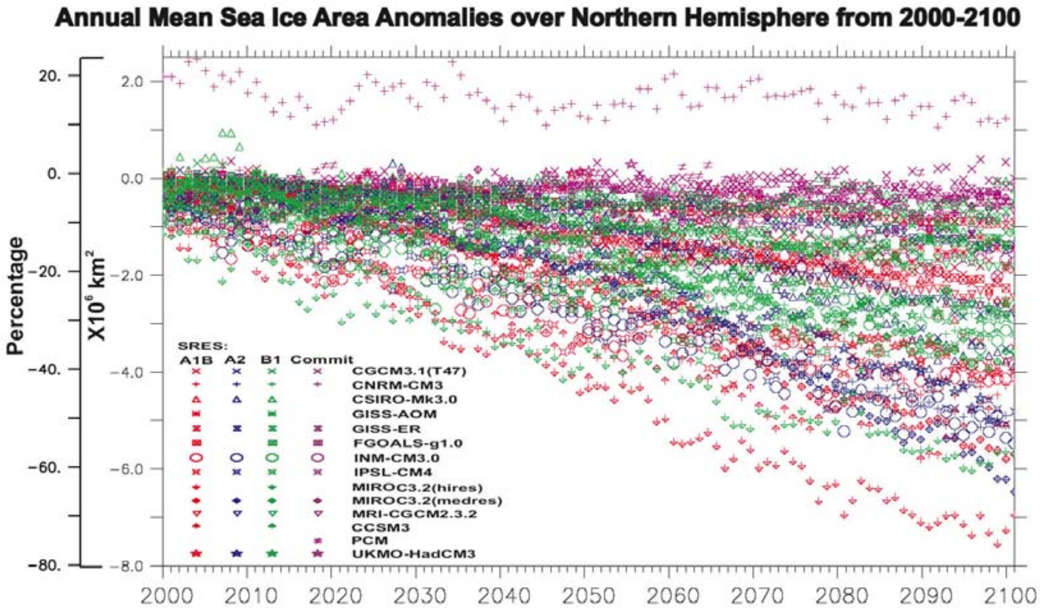

a)

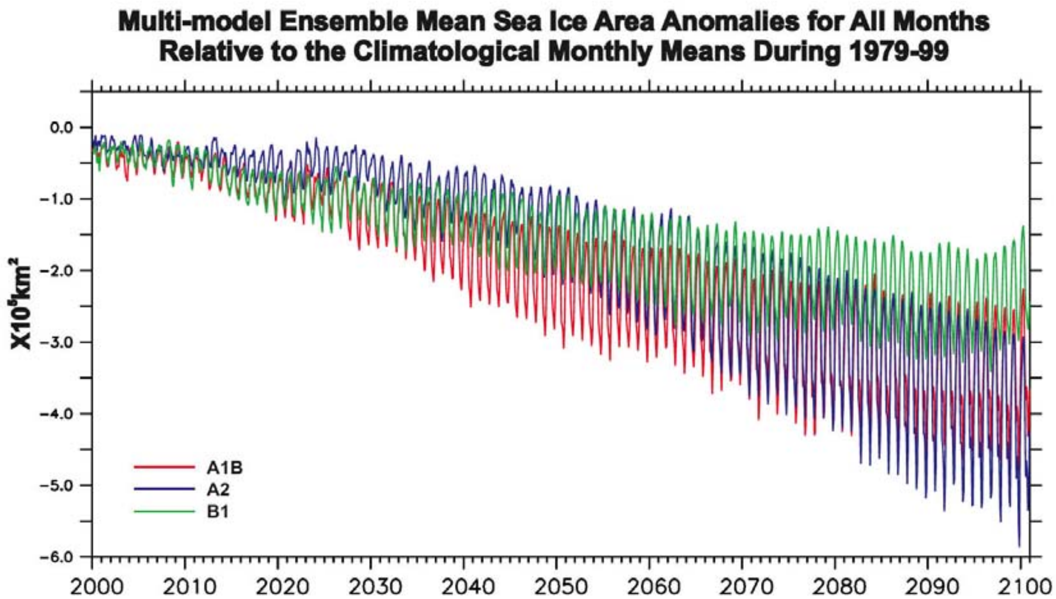

b)

Figure 10.3.10. a) Annual mean projected northern hemisphere sea ice area anomalies over the 21st century from all models forced by the SRES A1B, A2, and B1 scenarios. The anomalies were calculated by taking the difference of each individual model's projected sea ice area from the same model's 1979–1999 average. Also shown in a) is the percentage change after adjustment for biases in each model's 1979–1999 climatology. For completeness, results from a COMMIT experiment are included in which greenhouse gas levels are stabilised at 2000 levels throughout the entire 21st century. b) As in a) but for the multi model ensemble and each month over the 21st century. Notice that there is a trend towards increased seasonality under all three scenarios. There is no equivalent COMMIT curve in b). Annually-averaged and relative to the 1970-1999 model climatology, the reductions in b) are 31.1%, 33.4%, and 21.6%, at 2080–2100 for A1B, A2 and B1, respectively. Both a) and b) are taken from Zhang and Walsh (2005).

1980-1999 average *2080-2099 average*

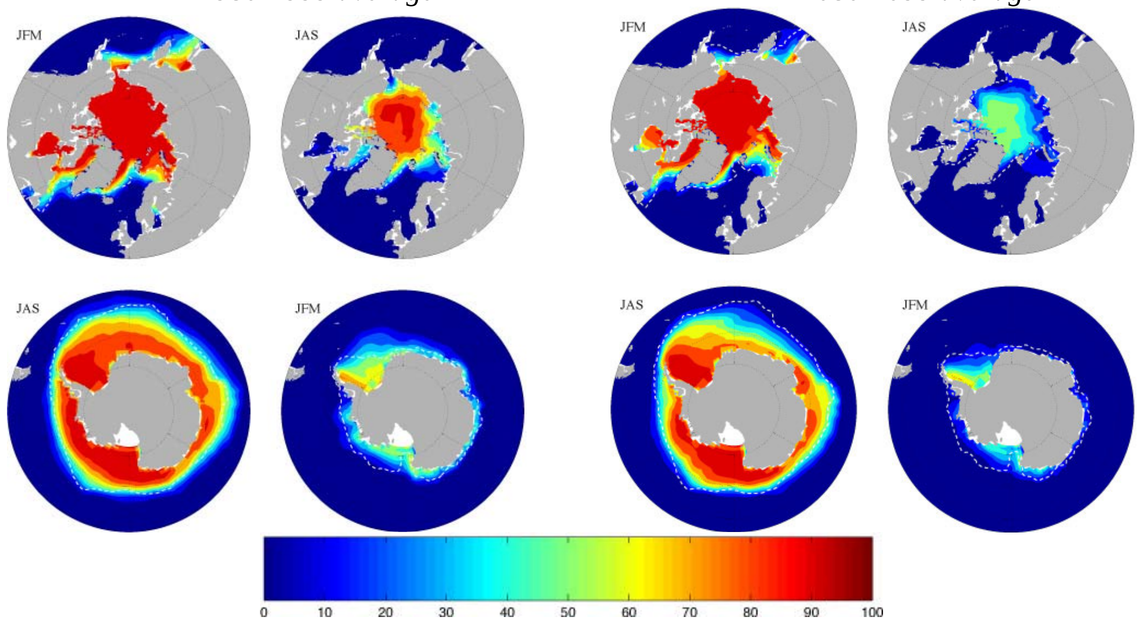

Figure 10.3.11. Multi-model average sea ice concentration (as percent) for JFM and JAS for present-day climate for the Arctic and Antarctic in the four left panels, and the sea ice distribution for the end of the 21st century from the A1B scenario in the four right panels. The dashed white line indicates the present-day 15% average sea-ice concentration limit. As in Flato et al. (2004) but updated using results from eight models: ukmo_hadcm3; mri_cgcm2_3_2a; giss_aom; ukmo_hadgem1; csiro_mk3_0; cnrm_cm3; cccma_cgcm3_1; CCSM3.

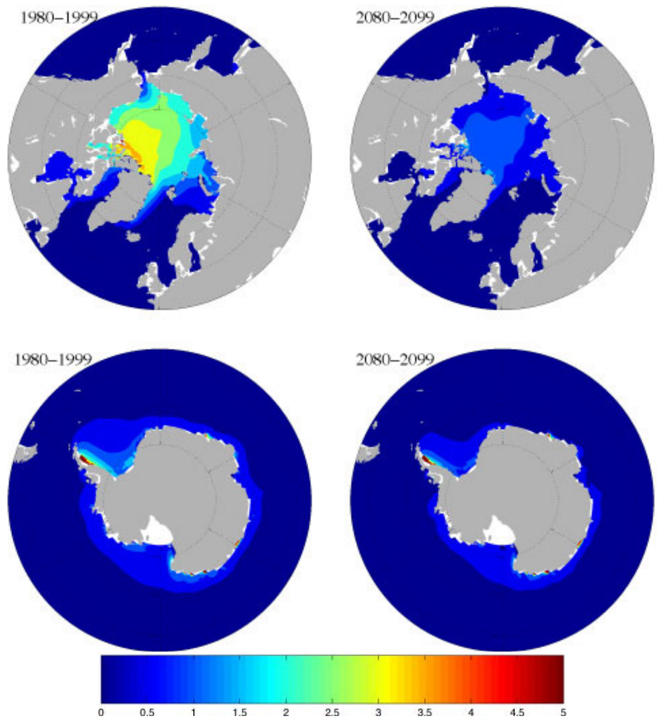

Figure 10.3.12. Multi-model average sea ice thickness (in meters) for all months for present-day climate (left) and for the end of the 21st century from the A1B scenario (right). As in Flato et al. (2004) but updated using results from eight models: ukmo_hadcm3; mri_cgcm2_3_2a; giss_aom; ukmo_hadgem1; csiro_mk3_0; cnrm_cm3; cccma_cgcm3_1; CCSM3.

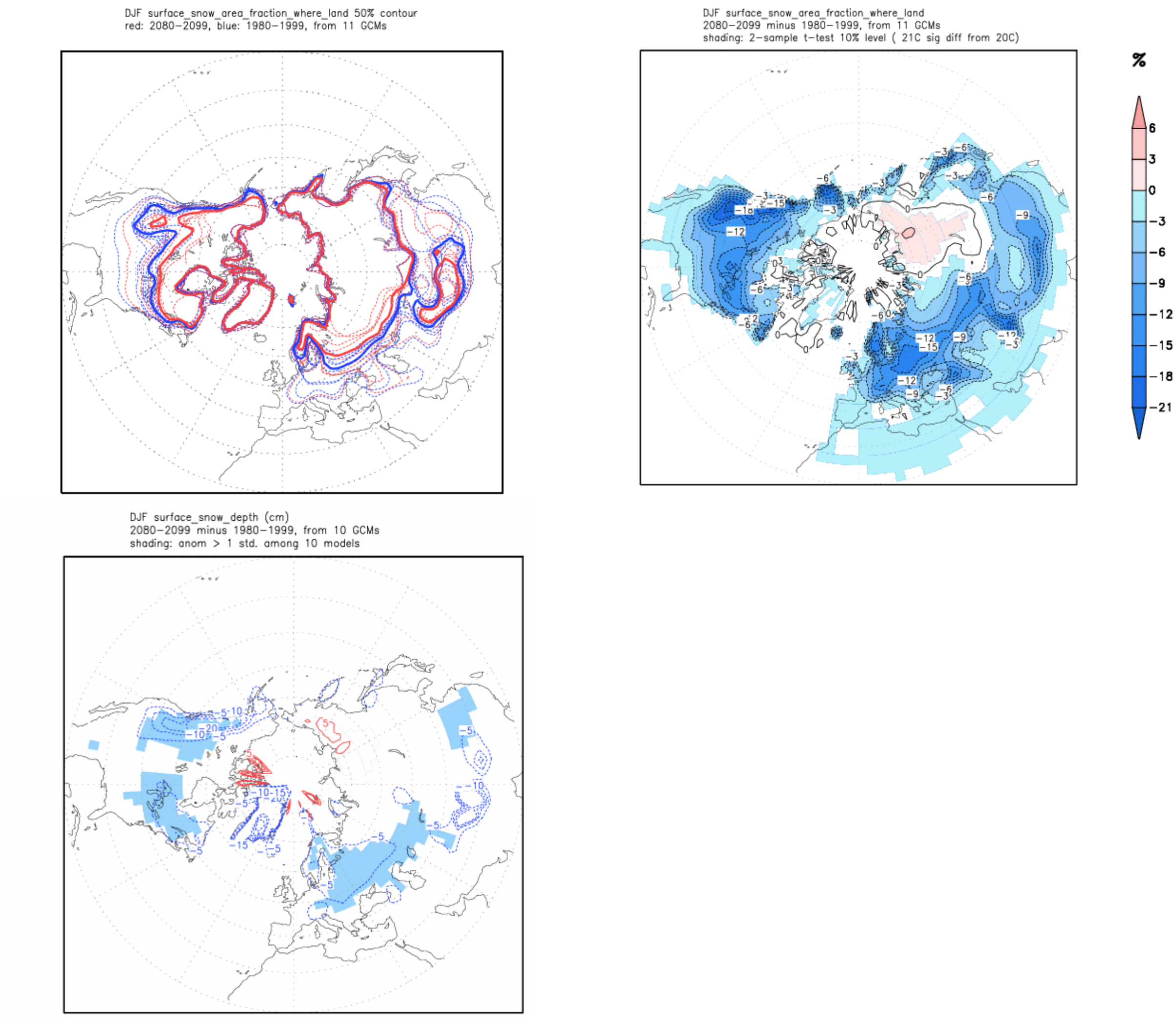

Figure 10.3.13. Multi-model average of snow cover and its changes during the 21st century from 11 GCMs. a): The contours give the locations where DJF snow cover exceeds 50%, blue for the period 1980–1999, and red for 2080–2099 and are dashed for the individual models and solid for the unweighted mean.
b): Contours of multi-model average of changes in snow cover area (changes given in %) between the periods 1980–1999 and 2080–2099. Significant changes (t-Test, 10% significance level) are colored.
c): Contours of multi-model average of changes in snow depth (changes given in cm) between the periods 1980–1999 and 20802099. Significant changes (t-Test, 10% significance level) are colored.

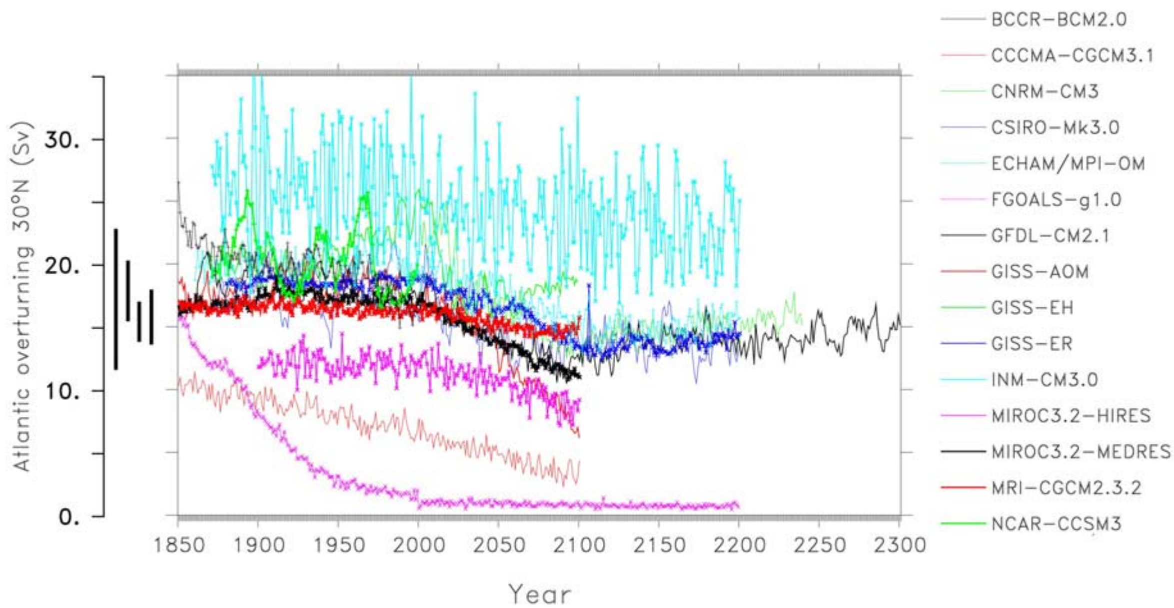

Figure 10.3.14. Evolution of the Atlantic meridional overturning circulation (MOC) at 30°N in simulations with the suite of comprehensive coupled climate models from 1850 to 2100 using emissions scenario SRES A1B. Some of the models continue the integration to year 2300 with the forcing held constant at the values of year 2100. Observationally based estimates of late 20th century MOC are given as vertical bars. Two models show a steady or rapid spin down of the MOC which is unrelated to the forcing; two others have late 20th century simulated values that are inconsistent with observational estimates. Of the model simulations consistent with the late 20th century observational estimates, no simulation shows an increase of MOC during the 21st century; reductions range from indistinguishable within the simulated natural variability to as much as 60% relative to the 1960–1990 mean; none of the models projects an abrupt transition to an off state of the MOC.